CANCER IMAGING

Hexachromatic bioinspired camera for image-guided cancer surgery

Steven Blair[1], Missael Garcia[1], Tyler Davis[1], Zhongmin Zhu[1], Zuodong Liang[1], Christian Konopka[2,3], Kevin Kauffman[4], Risto Colanceski[5], Imran Ferati[5], Borislav Kondov[5], Sinisa Stojanoski[6], Magdalena Bogdanovska Todorovska[7], Natasha Toleska Dimitrovska[5], Nexhat Jakupi[5], Daniela Miladinova[6], Gordana Petrusevska[7], Goran Kondov[5], Wawrzyniec Lawrence Dobrucki[2,3,8], Shuming Nie[1,2,9,10], Viktor Gruev[1,3,8]*

Cancer affects one in three people worldwide. Surgery remains the primary curative option for localized cancers, but good prognoses require complete removal of primary tumors and timely recognition of metastases. To expand surgical capabilities and enhance patient outcomes, we developed a six-channel color/near-infrared image sensor inspired by the mantis shrimp visual system that enabled near-infrared fluorescence image guidance during surgery. The mantis shrimp's unique eye, which maximizes the number of photons contributing to and the amount of information contained in each glimpse of its surroundings, is recapitulated in our single-chip imaging system that integrates arrays of vertically stacked silicon photodetectors and pixelated spectral filters. To provide information about tumor location unavailable from a single instrument, we tuned three color channels to permit an intuitive perspective of the surgical procedure and three near-infrared channels to permit multifunctional imaging of optical probes highlighting cancerous tissue. In nude athymic mice bearing human prostate tumors, our image sensor enabled simultaneous detection of two tumor-targeted fluorophores, distinguishing diseased from healthy tissue in an estimated 92% of cases. It also permitted extraction of near-infrared structured illumination enabling the mapping of the three-dimensional topography of tumors and surgical sites to within 1.2-mm error. In the operating room, during surgical resection in 18 patients with breast cancer, our image sensor further enabled sentinel lymph node mapping using clinically approved near-infrared fluorophores. The flexibility and performance afforded by this simple and compact architecture highlights the benefits of biologically inspired sensors in image-guided surgery.

INTRODUCTION

As humans have pursued rapid advancements in digital cameras, we have also found new biomedical applications for those cameras with surgical guidance provided by intraoperative imagers (*1*–*4*) and pathological samples identified by lab-on-a-chip devices (*5*). For diseases like cancer, where removal of primary tumors and confirmation of negative margins are critical to treatment, these aids to surgery and pathology offer great promise; however, there is a notable gap in the translation of many imaging technologies to clinical practice.

As an example, near-infrared fluorescence image-guided surgery has shown enormous potential for cancer surgery because of the low autofluorescence and scattering of tissues at near-infrared wavelengths, enabling large signal-to-background ratios and imaging depths while eschewing damaging ionizing radiation (*6*–*10*). With spectral sensitivity spanning the visible and near-infrared, digital cameras would seem well suited to color imaging of surgical sites and near-infrared imaging of fluorescently labeled tumors; however, state-of-the-art near-infrared fluorescence imaging systems suffer from complex architectures and narrow feature sets that have hindered adoption of next-generation tumor-targeted fluorophores as well as currently available nonspecific fluorophores. The first fluorescence-guided surgery was performed over 70 years ago (*11*), yet these issues have prevented near-infrared fluorescence image-guided surgery from being widely accepted as standard of care. Most physicians thus continue to rely on their unaided senses of sight and touch (*3*, *12*, *13*) which are, unfortunately, not optimized for the task: Incomplete tumor resection occurs in 25% of patients with breast cancer, 35% of patients with colon cancer, and 40% of patients with head and neck cancer (*14*). It would seem, then, that the solution to near-infrared fluorescence image-guided surgery lies somewhere between the digital cameras that engineering has manufactured and the eyes that biology has conceived.

The optimization of both manmade digital cameras and naturally evolved eyes has been driven by selection toward maximum fitness. Digital cameras have developed over several decades to satisfy consumers documenting daily life in real time and at high resolution (*15*), whereas eyes have evolved over millions of years to facilitate the complex decisions that permit survival of the species (*16*). Such divergent evolutionary pathways have created vastly different visual systems. Engineers have achieved frame rates and spatial resolutions that surpass nature (*17*) while offering quantum efficiencies, dynamic ranges, and signal-to-noise ratios that can be tuned over tremendous ranges. Biology has, in turn, seized the upper hand with visual systems that detect spectral information with extremely efficient and

[1]Department of Electrical and Computer Engineering, University of Illinois at Urbana-Champaign, Urbana, IL 61801, USA. [2]Department of Bioengineering, University of Illinois at Urbana-Champaign, Urbana, IL 61801, USA. [3]Beckman Institute for Advanced Science and Technology, University of Illinois at Urbana-Champaign, Urbana, IL 61801, USA. [4]Department of Biomedical Engineering, University of Michigan, Ann Arbor, MI 48109, USA. [5]University Clinic Hospital, Department of Thoracic and Vascular Surgery, Ss. Cyril and Methodius University of Skopje, 1000 Skopje, Republic of North Macedonia. [6]University Clinic Hospital, Institute of Pathophysiology and Nuclear Medicine, Ss. Cyril and Methodius University of Skopje, 1000 Skopje, Republic of North Macedonia. [7]University Clinic Hospital, Department of Pathology, Ss. Cyril and Methodius University of Skopje, 1000 Skopje, Republic of North Macedonia. [8]Carle Illinois College of Medicine, University of Illinois at Urbana-Champaign, Urbana, IL 61820, USA. [9]Department of Chemistry, University of Illinois at Urbana-Champaign, Urbana, IL 61801, USA. [10]Department of Materials Science and Engineering, University of Illinois at Urbana-Champaign, Urbana, IL 61801, USA.
*Corresponding author. Email: vgruev@illinois.edu

effective architectures (*18*, *19*); for example, the mantis shrimp visual system, which fits 16 types of cone cells onto compact eyestalks, is unmatched by any manmade spectral camera in power consumption and information density. The marriage of the optimized optoelectronics built into digital cameras and the diverse functionality observed in eyes has borne imaging systems with sensory capabilities exceeding those previously provided by engineers and biology alike (*10*, *20*, *21*), suggesting a future for near-infrared fluorescence image-guided surgery.

RESULTS

A bioinspired image sensor for near-infrared fluorescence image-guided surgery

Two key trends jeopardize potential solutions for near-infrared fluorescence image-guided surgery. The first trend involves architectures: Existing instruments rely on two architectures that are poorly matched to the clinical context (table S1). In division-of-time architectures, a filter wheel isolates different spectral channels at different times, permitting all spectral channels to be captured by the same image sensor at distinct time points. This collection of spectral information over time requires reduced exposure times with increasing channel counts, maintaining real-time frame rates but reducing fluorescence signal-to-noise ratios, and introduces co-registration error between spectral channels because of interframe motion. In division-of-optical-path architectures, dichroic beamsplitters or dichroic/trichroic prisms direct different spectral channels along different optical paths, permitting all spectral channels to be captured by distinct image sensors at the same time point. This collection of spectral information across space guarantees increased device sizes with increasing channel counts, demanding additional relay optics that affect image quality. The second trend involves feature sets: Existing instruments typically image a single fluorescent probe (tables S1 and S2), providing insufficient sensitivity and specificity for real physiology. Because of variations in inter- and intratumor biomarkers, a single tumor-targeted probe may fail to detect metastatic tumors or may fail to detect the boundaries of primary tumors. This was confirmed by a recent meta-analysis indicating that up to 40% of metastatic tumors and involved lymph nodes can have biomarkers different from those of the primary tumor (*22*).

To address these issues, we turned to the mantis shrimp visual system as a blueprint for an artificial image sensor. The mantis shrimp benefits from a simple physical phenomenon that imbues spectral sensitivity: Shorter-wavelength photons (i.e., blue light) penetrate shorter distances into their compound eyes than do longer-wavelength photons (i.e., red light) because of a wavelength-dependent absorption coefficient (*23*). As a result, the photosensitive cells at the top of the mantis shrimp's compound eyes preferentially register shorter-wavelength photons, whereas the photosensitive cells at the bottom preferentially register longer-wavelength photons (Fig. 1, A and B). Crystalline cones above the compound eye provide fine-grained spectral filtering, enabling different parts of the eye to see different bands of light (Fig. 1, A and B). Ultimately, this unique combination of vertically stacked photodetectors with spectral filters enables 16 spatiotemporally co-registered spectral bands to be constantly probed by microscopic cells, offering increased optical throughput as multiple spectral observations are made without rejecting photons, increased data throughput as multiple spectral observations are made at every point, and increased spatial resolution as spectral observations are distributed vertically as well as laterally.

To mimic the mantis shrimp's multispectral capabilities, we designed and fabricated an image sensor by monolithically integrating an array of vertically stacked silicon photodetectors with an array of pixelated spectral filters (Fig. 1, C and D). The absorption length of silicon strongly varies with wavelength, with 99% of blue photons (~400 nm) absorbed within 0.5 μm of penetration and 99% of red photons (~650 nm) absorbed within 16 μm of penetration. Recognizing the high density of photocharge generation by blue photons in a thin sheet near the surface and by red photons in a thick slab farther below the surface, the location and extent of photodiodes in the silicon can be selected to measure the amounts of blue and red light in a scene: A blue-sensitive photodiode is shallow and of limited extent, whereas a red-sensitive photodiode is deeper and of greater extent. Green photons experience an intermediate absorption coefficient and can be detected with an intermediate photodiode. The spectrum of incident photons can be further shaped with spectral filters, enabling a wide range of distinct responses.

An array of vertically stacked photodiodes was fabricated by epitaxial growth of three positively doped (p+) silicon layers with individual thicknesses of 0.8, 2.8, and 4.3 μm, followed by ion implantation to generate negatively doped (n+) regions (Fig. 1, C and D). The photodiodes were most responsive at ~430, ~550, and ~700 nm but maintained responsiveness at longer wavelengths. An array of pixelated spectral filters was produced by stacking submicrometer layers of the dielectric materials silicon dioxide, silicon nitride, and hafnium oxide in different quantities and thicknesses on a glass substrate (Fig. 1, C to F). The filters were organized in an alternating grid of short-pass filters, with passbands below 700 nm, and long-pass filters, with passbands above 700 nm. The monolithically integrated image sensor was finally produced by flip-chip bonding the arrays of vertically stacked photodiodes and pixelated spectral filters (Fig. 1, C and D).

Optoelectronic characterization

The spectral response of the complete image sensor was benefitted by the high in-band transmission (~95%) and high out-of-band rejection (optical density ~4) of the pixelated spectral filters (Fig. 2A). The three photodiode layers under the short-pass filters maintained distinct spectral responses that peaked under blue, green, and red light; the three photodiode layers under the long-pass filters exhibited similar spectral responses that peaked at ~700 nm (Fig. 2B), but the differences in the spectral responses across the photodiode layers were substantial enough to enable three different observations of the near-infrared spectrum. Together, the three visible channels under the short-pass filters and the three near-infrared channels under the long-pass filters accounted for a total of six spectral channels—providing hexachromatic vision. As needed, additional notch filters (optical density >6) were placed over the whole sensor to suppress photons from the excitation light sources.

The stacked photodiodes' spectral responses compared favorably against scientific cameras optimized for color reproduction, with the centroid wavelengths of our imaging system's color channels (i.e., 507, 563, and 607 nm) (Fig. 2B) falling near those of Teledyne QImaging's MicroPublisher 6's color channels (i.e., 464, 540, and 608 nm) (*24*). This correspondence was confirmed in color images (like that in fig. S1) where complex natural scenes with diverse color content appeared natural. The optimization toward broadly shaped

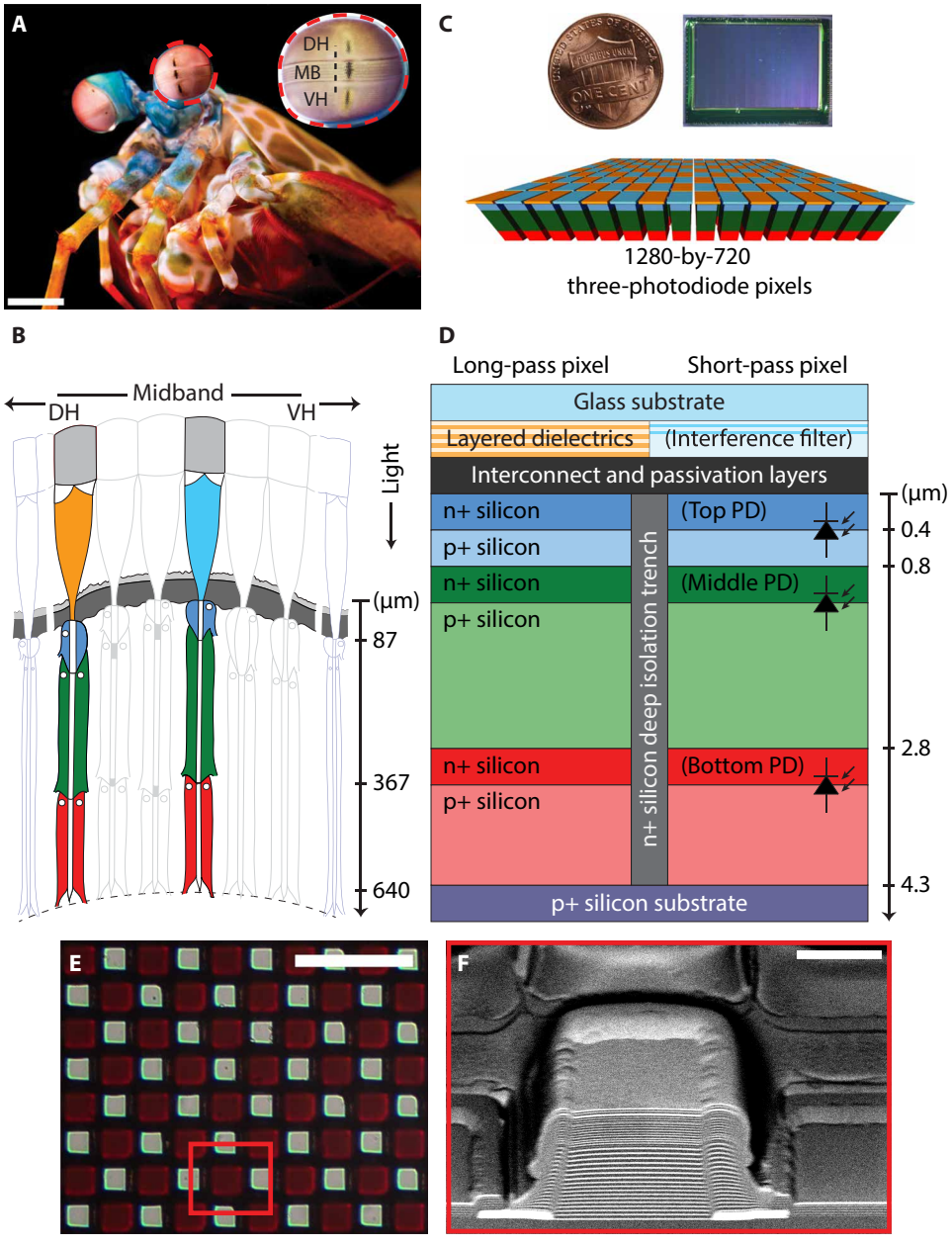

Fig. 1. Comparison of the mantis shrimp compound eye and the bioinspired image sensor. (**A**) Photograph of the mantis shrimp *Odontodactylus scyllarus* and magnified photograph of its compound eye (inset); scale bar, 5 mm. (**B**) A cross-section of the compound eye of the mantis shrimp *Gonodactylus chiragra* shows the photosensitive cells and spectral filters; structures without dimensions are not to scale. The photosensitive cells at the bottom, middle, and top have been colored red, green, and blue, respectively, to emphasize that longer wavelengths of light penetrate farther than shorter wavelengths. (**C**) Photograph of the bioinspired imager (top) and magnified illustration of the pixel array (bottom); scale is indicated by the penny. (**D**) A cross-section of the bioinspired imager shows the vertically stacked photodiodes, composed of layers of n-doped silicon and p-doped silicon, and the interference filters, composed of layers of different dielectric materials; structures without dimensions are not to scale. The photodiodes at the bottom, middle, and top have been colored red, green, and blue, respectively, to emphasize that longer wavelengths of light are absorbed deeper in the silicon than shorter wavelengths. (**E**) An optical microscope image of the pixelated optical filters shows the long-pass filters as dark colored squares and the short-pass filters as bright colored squares; scale bar, 50 μm. (**F**) A scanning electron microscope image depicts a long-pass filter in the center and short-pass filters on both sides; scale bar, 5 μm. (A) Credit: Michael Bok, University of Lund. In (B), the cross-section is adapted from (*23*). In (C) and (D), the magnified illustration and cross-section present a conceptual view of the device, omitting some details for clarity. DH, dorsal hemisphere; MB, midband; PD, photodiode; VH, ventral hemisphere.

quantum efficiencies in the visible spectrum ensured sufficient shaping in the spectral responses at the shorter end of the near-infrared spectrum, allowing the U.S. Food and Drug Administration–approved fluorescent dyes methylene blue (MB) ($\lambda_{em} \approx 690$ nm) and indocyanine green (ICG) ($\lambda_{em} \approx 810$ nm) to induce different signals. Nevertheless, the location and extent of the bottom photodiode offered a benefit farther into the near-infrared spectrum where the spectral response did not degrade until beyond 1000 nm (Fig. 2B), providing a meaningful increase for weak fluorescent signals at the expense of a computationally correctable red hue in color images. Further tuning of the photodiode parameters would enable an application-specific trade-off between color accuracy and near-infrared discrimination when the selected parameters prove insufficient while maintaining the additional benefits to optical throughput, data throughput, and spatial resolution afforded by the stacked photodiodes.

The image sensor exhibited a read noise of 62 electrons and a linear full well capacity of 101,473 electrons at the middle photodiode, indicating a dynamic range of 64 dB or 10.7 bits at this worst-case photodiode; furthermore, the image sensor exhibited a maximum fixed pattern noise of 0.6% at half the linear full-scale range (Fig. 2C). Both the read noise and the fixed pattern noise were affected by difference double sampling within the readout circuit: At the price of an effective doubling of the read noise at each pixel, there was a substantial drop in threshold voltage variation across the image sensor. An additional charge-transfer transistor, a pinning layer, and a floating diffusion for each photodiode would permit correlated double sampling, which would simultaneously reduce read noise and correct offsets, as demonstrated in other complementary metal-oxide-semiconductor (CMOS) fabrication processes using embedded photodiodes (*25*, *26*). The dark current of the image sensor was 4107 electrons per second in the worst case at the top photodiode; however, the requirements for image-guided surgery often included a real-time frame rate of ~25 frames per second (~40 ms per frame), limiting the quantity of dark charge that could be accumulated and the power of dark noise

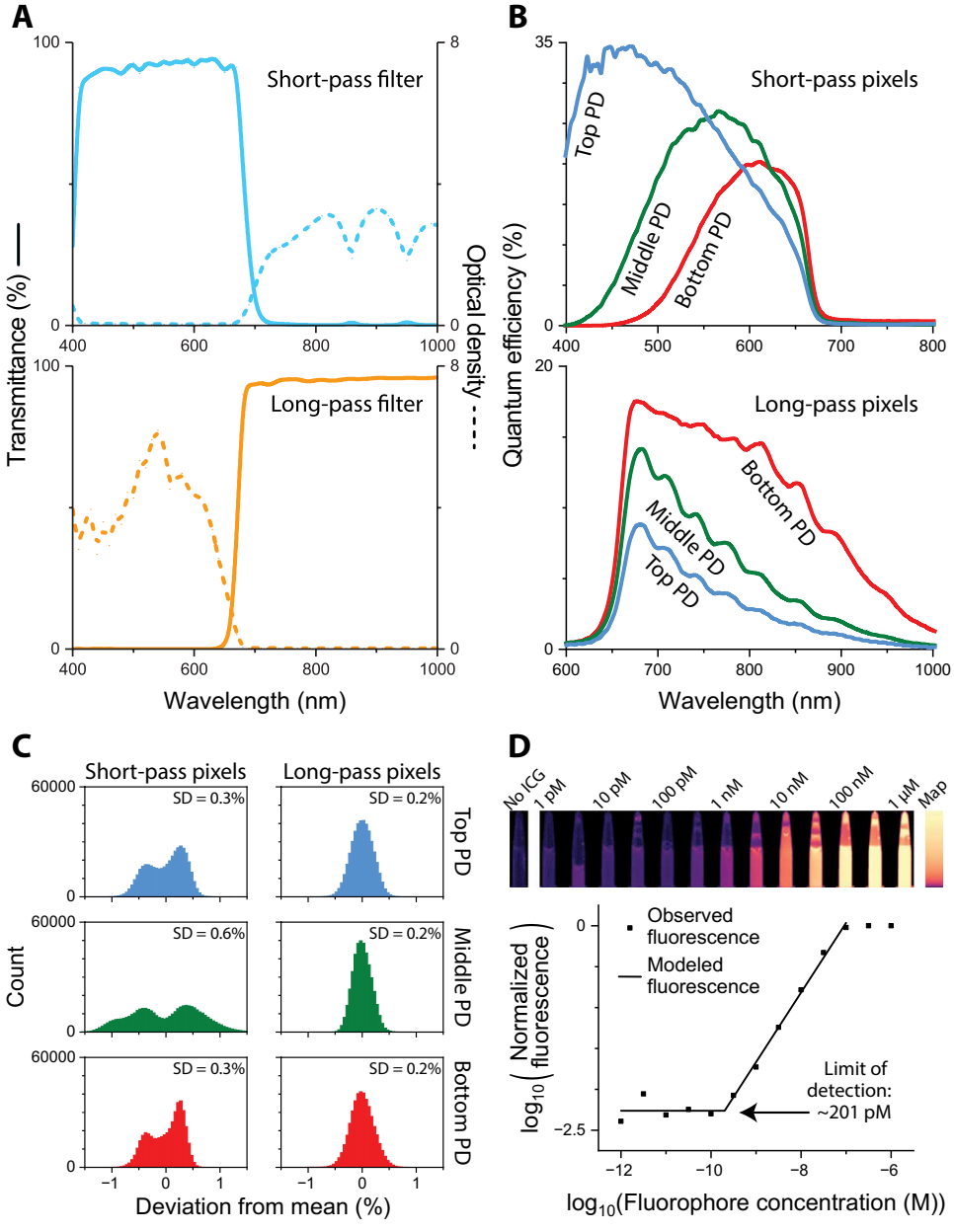

Fig. 2. Optoelectronic characteristics of the bioinspired imager. (**A**) Transmission and optical density curves for the short-pass filters (top) and long-pass filters (bottom). (**B**) Quantum efficiency curves for the three photodiode layers under the short-pass filters (top) and long-pass filters (bottom). (**C**) Fixed pattern noise histograms at half the linear full-scale range for the three photodiode layers under the short-pass filters (left) and long-pass filters (right). The fixed pattern noise is the SD of the histograms. (**D**) Normalized fluorescence observed and modeled across different concentrations of indocyanine green (ICG). Temporally averaged intensity images are displayed against concentration (top), and spatiotemporally averaged intensities are plotted against concentration (bottom). The detection limit (201 pM) is the transition point between the constant region below the noise floor and the linear region above the noise floor. PD, photodiode.

200-ms integration time under 780-nm laser excitation (20 mW/cm^2) (Fig. 2D).

Intraoperative imaging of cancers requires simultaneous recording of the plentiful visible photons that outline a patient's anatomical features and the sparse fluorescent photons that highlight the locations of tumors. Visible photons from the surgical lighting undergo a single reflection at the surface of the surgical site before entering the imaging system, whereas near-infrared photons from the fluorescence excitation undergo a complex series of scattering, absorption, excitation, and emission events before collection, ensuring that the fluorescent photons experience far more losses. However, the International Electrotechnical Commission has specified a lower bound on the illuminance of surgical lighting and an upper bound on the irradiance of fluorescence excitation that prevents changes to the light sources sufficient to overcome such losses (*27*, *28*). These asymmetries in optical paths and lighting specifications yield a large dynamic range between the strong visible lighting and the weak fluorescent signal that exceeds ~90 dB in the best case, beyond the 80-dB capability of state-of-the-art sensors. Even if sufficiently large dynamic ranges could be achieved in conventional sensors, for example, by reducing the readout noise and increasing the full well depth, the requirement that the color image remain unsaturated would practically guarantee that the near-infrared image would occupy the lower half of the dynamic range. Because of the Poisson distribution of the shot noise, the signal-to-noise ratio of the near-infrared image would be minimal, increasing the risk that weakly labeled fluorescent targets may not be detected. As a result, our image sensor included programmable readout circuitry that independently controlled the exposure times for the color pixels and near-infrared pixels. This enabled our image sensor to simultaneously acquire high signal-to-noise ratio images in both the visible and near-infrared spectra.

that could be observed after any single exposure. Therefore, common corrections like image sensor cooling would yield a minimal reduction in an already small dark current, producing little improvement in the accumulated dark charge, the observed dark noise, and the resulting signal-to-noise ratio. The quantum efficiencies coupled with this noise performance permitted detection of 201 pM ICG at

Simultaneous imaging of multiple near-infrared fluorescent signals

The most important information about the near-infrared spectrum was encoded in the comparative variation across and the overall intensity of the near-infrared channels, not the absolute value of each channel; thus, a transformation was required to map the measured

photodiode response to a more intuitive quantity. In practice, the transformation from red-green-blue (RGB) to hue-saturation-value (HSV) used in color image processing proved adept at separating different signals encoded in the near-infrared channels. Under this transformation, hue and saturation represented ratios of differences between the three channels, providing information about the incident spectrum, whereas value represented the response of the strongest channel, providing information about the incident intensity. Together, hue and saturation enabled differentiation of multiple targets (e.g., two fluorescent markers) based on the targets' spectral characteristics (e.g., different emission wavelengths), whereas value permitted a comparison between the targets' intensities. At the same time, value measured the targets' intensities with maximal signal-to-noise ratio and was preferred when the overall intensity of multiple dyes, not the differences between those dyes, was of interest during decision making. Even without the physical meaning of the total energy across spectral bands, these abstract quantities of hue, saturation, and value permitted application-specific descriptions for image-guided surgery while enabling full use of the near-infrared measurements at each pixel. Images could thus be formed from either the raw quantities or informative transformations of them and presented to the surgical staff on a display.

To demonstrate that the image sensor was sensitive to small perturbations of the incident spectrum, we prepared the near-infrared fluorophore ICG in two different solvents, deionized water and fetal bovine serum. When excited with the same light source, the emission peaks from these samples were spectrally separated by 8 nm, but the emission spectra from these samples were clearly distinguished by our image sensor, as evidenced by the separation between the 95% tolerance ellipses for the hues and saturations (Fig. 3A). To

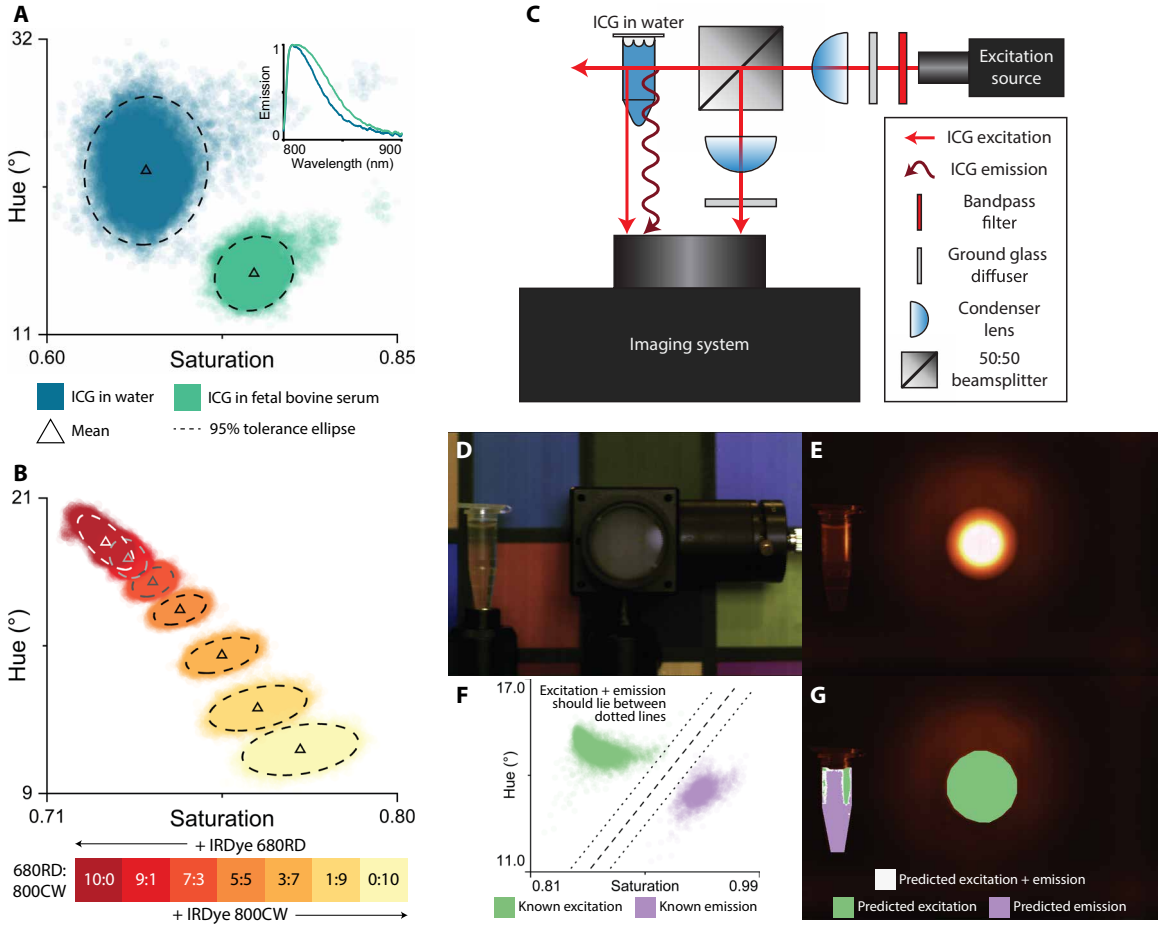

Fig. 3. Imaging capabilities of the bioinspired imager. (**A**) Discrimination of indocyanine green (ICG) diluted in two different media (deionized water and fetal bovine serum) showing the uncertainty created by temporal and spatial noise. Observations of different solutions appear in different clusters and are circled by 95% tolerance ellipses ($n_{observations}$ = 27,000 per solution). Emission spectra for the two solutions are displayed in the top-right inset. (**B**) Discrimination of IRDye 680RD and IRDye 800CW mixed in different volumetric ratios showing the uncertainty created by temporal and spatial noise. Observations of different ratios appear in different clusters and are circled by 95% tolerance ellipses ($n_{observations}$ = 27,000 per solution). Emission spectra for IRDye 680RD and IRDye 800CW are strongest at ~694 and ~794 nm, respectively. (**C** to **G**) Discrimination of ICG excitation and emission in the presence of spatial noise. (C and D) Schematic (C) and color photograph (D) of the experimental setup. Excitation is projected from the port; emission is generated in and excitation is reflected from the vial. (E) Near-infrared image of the experimental setup. Pure excitation is observed inside the port; pure excitation, pure emission, and mixed excitation-emission are observed inside the vial. (F) Temporally averaged observations of pure excitation and pure emission cluster differently, permitting classification via a simple margin classifier such as a linear support vector machine ($n_{observations}$ = 8246 for excitation and 2665 for emission). Observations of mixed excitation-emission should lie between and are classified accordingly. (G) Labels of pure excitation, pure emission, and mixed excitation-emission can be applied to the near-infrared image using the classifier.

illustrate further that the hue-saturation response varied continuously with a smooth change in the incident spectrum, we prepared the near-infrared fluorophores IRDye 680RD and IRDye 800CW in seven volumetric ratios from 10-to-0 to 0-to-10. When excited with two light sources, the single degree of freedom in volumetric ratios dictated that the emitted spectrum from the fluorophore mixture was the volume-weighted average of the emission spectra from the individual fluorophores; as expected, our image sensor returned hues and saturations confined about a one-dimensional manifold with limited overlap between the 95% tolerance ellipses associated with different ratios (Fig. 3B), permitting quantification of the relative concentrations of the two dyes. Both of these results were achieved because of the spectral sensitivity, temporal noise performance, and spatial noise performance of the imaging system.

The image sensor's ability to distinguish emission spectra has notable applications, but its ability to differentiate emission spectra from excitation spectra is also important. Given that the hue and saturation provide information about the incident spectrum, and that the fluorescent excitation spectrum and the fluorescent emission spectrum are always different, the reflection from an excitation light source and the emission from a fluorophore map to different hue-saturation points, permitting discrimination in the hue-saturation space. This has applications in surgery, where the small number of excitation photons that reflect from the surgical site and pass through the emission filter compete with the potentially small number of emission photons that reach the image sensor. A divergence in response was exhibited in the benchtop experiment shown in Fig. 3 (C to G), where pixels exposed only to fluorescence excitation or fluorescence emission laid in separate clusters in the hue-saturation space and pixels exposed to a mixture of excitation and emission laid between. This permitted labeling of pixels that were useful (observed mostly emission), useless (observed mostly excitation), and of potential use (observed a mixture of emission and excitation).

Tumor detection in a small-animal model of human prostate cancer

To evaluate the sensitivity to and utility of multiple fluorophores in a surgical context, our imaging system was used to identify fluorescently labeled tumors in a small-animal model of human prostate cancer. Human prostate cancer cells (LNCaP and PC3) were subcutaneously implanted in nude athymic mice, and ~2 weeks later, two near-infrared fluorescent optical probes [IRDye 680RD, labeled with human recombinant epidermal growth factor (EGF), and IRDye 800CW, labeled with 2-deoxy-D-glucose (2-DG)] were intravenously injected into the same mice. After 24 hours, the mice underwent whole-body fluorescent imaging with our imaging system before the tumor and healthy tissues were surgically removed and imaged separately. Imaging occurred under 665-nm excitation (targeting IRDye 680RD EGF), 780-nm excitation (targeting IRDye 800CW 2-DG), and mixed 665 nm–780 nm excitation (targeting both IRDye 680RD EGF and IRDye 800CW 2-DG).

Using the near-infrared information from our imaging system, each tissue sample was scored and classified as either tumor tissue or healthy tissue, and these predictions were compared against ground truth. Receiver operating characteristic (ROC) curves (Fig. 4A and data file S1) indicated an area under the curve (AUC) of 0.92 under mixed 665 nm–780 nm excitation (IRDye 680RD EGF and IRDye 800CW 2-DG together) compared to 0.77 for 665-nm excitation (IRDye 680RD EGF alone) and 0.75 for 780-nm excitation (IRDye 800CW 2-DG alone). Accounting for the paired design of the imaging study, a dual-tracer strategy using EGF and 2-DG together significantly outperformed single-tracer use of EGF ($P = 0.022$) and single-tracer use

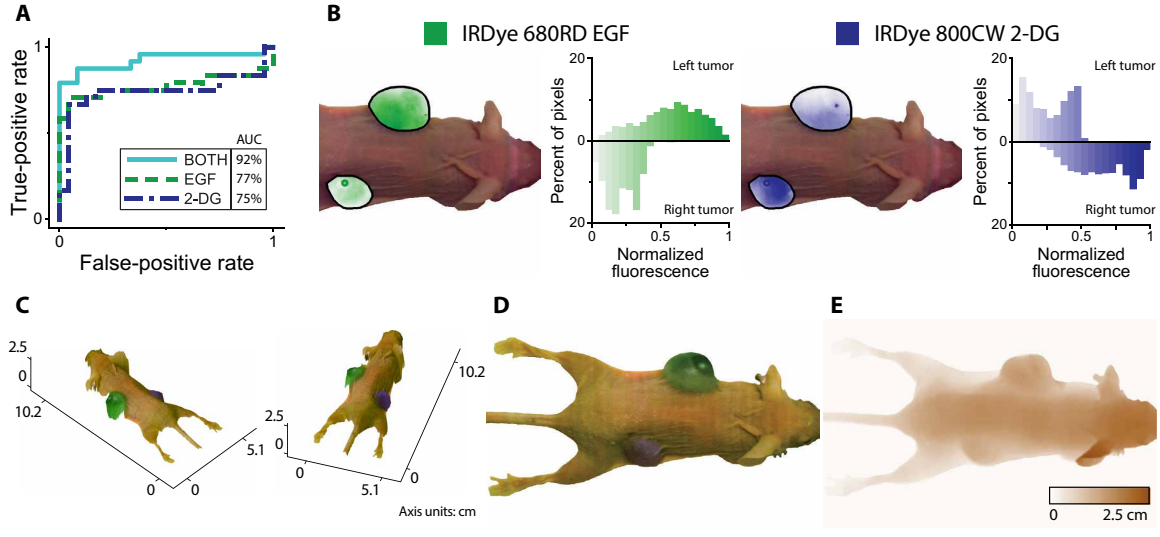

Fig. 4. Human tumor detection in nude mice using the bioinspired imaging sensor. (**A**) Receiver operating characteristic (ROC) curves for tumor detection in mice using the two dyes IRDye 680RD epidermal growth factor (EGF) and IRDye 800CW 2-deoxy-D-glucose (2-DG) together or each dye alone. Area under the curve (AUC) improves for two dyes compared to one dye ($P < 0.05$; $n_{tumor} = 24$, $n_{healthy} = 24$). (**B**) Normalized fluorescence from human PC3 prostate tumors in a nude athymic mouse overlaid on a color image and plotted in a histogram. IRDye 680RD EGF (left) and IRDye 800CW 2-DG (right) are taken up by the two tumors, but the dyes exhibit substantial heterogeneity between and within those tumors. IRDye 680RD EGF dominates in the left tumor, whereas IRDye 800CW 2-DG dominates in the right tumor. (**C**) Two color images of the same tumor-bearing mouse showing the estimated three-dimensional profile with the tumors highlighted and the dominant targeted probes indicated (see movie S1). (**D**) Color image of the tumor-bearing mouse showing the tumors highlighted along with the dominant targeted probes as indicated by normalized fluorescence. (**E**) Three-dimensional profile of the tumor-bearing mouse indicating the out-of-plane height as extracted from structured illumination.

of 2-DG ($P = 0.016$) when comparing AUCs. Considering the difference between the AUC for the EGF plus 2-DG scenario and the AUCs for the single-tracer scenarios, the 95% confidence interval was (0.03 to 0.29) for the EGF scenario and (0.04 to 0.36) for the 2-DG scenario, indicating a statistically significant improvement in tumor scoring.

Images composited from color and near-infrared observations of a mouse along with histograms computed from near-infrared observations within its tumors are provided in Fig. 4B. Although IRDye 680RD EGF and IRDye 800CW 2-DG were taken up by two tumors, the tracers exhibited substantial heterogeneity between and within those tumors. IRDye 680RD EGF produced a consistently stronger fluorescent signal in the tumor on the left flank than in the tumor on the right flank, whereas IRDye 800CW 2-DG behaved in the opposite way, producing a stronger signal in the right tumor than in the left tumor. Regardless of the overall brightness, the dyes produced a stronger signal in some regions and a weaker signal in others, with the intensity generally dropping from the medial region of the tumors to the lateral region. The application of a dual-tracer strategy would counteract the heterogeneity of these single-tracer strategies. In some cases, the two tracers would complement each other, with one tracer accentuating tissues missed by the other tracer; in other cases, the two tracers would supplement each other, with both tracers emphasizing similar cues that should improve confidence in surgical decision making.

All three visible channels were required for color imaging of the surgical site, while two near-infrared channels were required for near-infrared imaging of the fluorescent dyes (IRDye 680RD EGF with $\lambda_{em} \approx 693$ nm and IRDye 800CW 2-DG with $\lambda_{em} \approx 780$ nm), accounting for five of the image sensor's spectral channels. The third near-infrared channel was dedicated to three-dimensional reconstruction using structured illumination from a near-infrared projector (at $\lambda \approx 900$ nm), ensuring full use of all six channels. The projector illuminated the surgical site with a sinusoidal pattern advancing along the wavefront normal, while an algorithm compared the observed phase change to the expected phase change and extracted that part of the phase change induced by the three-dimensional topography; an inverse model then facilitated conversion of these phase changes into a height map. These three-dimensional reconstructions could be generated at a spatial resolution of 1280 pixels × 720 pixels and a frame rate of 30 frames per second while exhibiting an average root mean square error of 1.179 mm and an average signal-to-noise ratio of 36.

Figure 4C shows representative images of a tumor-bearing mouse before surgery indicating both the fluorescently labeled tumors and the three-dimensional reconstruction; an animation of these images is provided in movie S1. Three visible channels worth of information were used to visualize the mouse, while two near-infrared channels worth of information were used to detect the tumors (Fig. 4D); the remaining near-infrared channel worth of information was used to extract the shape of the mouse and the tumors within the mouse (Fig. 4E). The tumors were highlighted in either green or blue to emphasize preferential accumulation of either IRDye 680RD EGF or IRDye 800CW 2-DG as measured by normalized fluorescence under 665- or 780-nm excitation, emphasizing that different tumors may be more easily detected with different dyes (Fig. 4, C and D). In the operating room, however, the tumors would normally be identified together under mixed 665 nm–780 nm illumination, permitting the greater diagnostic performance demonstrated by the ROC analysis (Fig. 4A). This diagnostic information, coupled with inherently co-registered shape information, may improve tumor detection despite inter- and intratumoral variations and optimize surgical strategies according to the tumors' size and extent.

Clinical feasibility of sentinel lymph node detection in patients with breast cancer

To explore translation of a multifluorophore workflow to a clinical environment, our imaging system was used to visualize fluorescently labeled sentinel lymph nodes in patients with early-stage breast cancer. In conventional surgical practice, sentinel lymph node mapping involves the peritumoral administration of radioactive tracers like technetium-99m–labeled human serum albumin colloid (^{99m}Tc-HSA colloid) that can be identified with a gamma probe and dark-colored dyes like ICG and MB that can be observed with the naked eye. Given that ICG and MB are both near-infrared fluorophores, though, it is possible to detect these dyes by their near-infrared fluorescence, enabling identification of sentinel lymph nodes without the radioactivity associated with radiotracers and the limited depth of visualization associated with visible stains. According to the standard of care, ^{99m}Tc-HSA colloid, MB, and ICG were administered before breast cancer surgery. On the basis of radioactive signals and visual cues, all suspected lymph nodes were removed from the patient and imaged with our imaging system under 780-nm excitation (for ICG detection), 665-nm excitation (for MB detection), and mixed 780 nm–665 nm excitation (for dual ICG and MB detection). Immediately thereafter, the suspected lymph nodes underwent histopathologic analysis to determine whether the resected tissues were lymphatic structures and to evaluate whether they exhibited metastases.

A photograph of our imaging system in the operating room is provided in Fig. 5A. Representative images of sentinel lymph nodes in vivo during and ex vivo after surgery are provided in Fig. 5 (B to F), and a video of a sentinel lymph node resection is provided in movie S2. In vivo, ICG and MB collected in different regions of the surgical site at different moments during the operation. From the injection of the dyes through the massage of the tissues to the beginning of resection, the dyes migrated from the injection site to the lymph node as scalpels, retractors, and other tools were introduced throughout the procedure. In such a dynamic environment, where fluorophores were covered and uncovered, modulating the fluorescent emission, and where tools were constantly moving, absorbing, and reflecting the fluorescent excitation, it was critical that relevant fluorescent emission be detected and that irrelevant fluorescent excitation be rejected, all while under surgical illumination. Our imaging system, which could detect weak fluorescence emission and differentiate between fluorescence emission and excitation, identified lymph nodes under such demands. Ex vivo, ICG and MB concentrated at different points in different lymph nodes. As the dyes traveled through the lymphatic basin into a lymph node, they exhibited differences in accumulation based on disparities in molecular weight, hydrodynamic radius, and charge; such variation could cause one dye to exhibit a homogeneous response and another dye a highly heterogeneous response, although both dyes were injected at a similar time and place. Again, our imaging system, which could spectrally differentiate the dyes and use that spectral information for application, identified lymph nodes in such a context.

Ultimately, our imaging system succeeded at detecting sentinel lymph nodes, providing an AUC of 88% for ex vivo samples with ICG, as well as a true-positive rate of 84% and a false-positive rate of 0% at maximal Youden's index (Table 1 and data file S2).

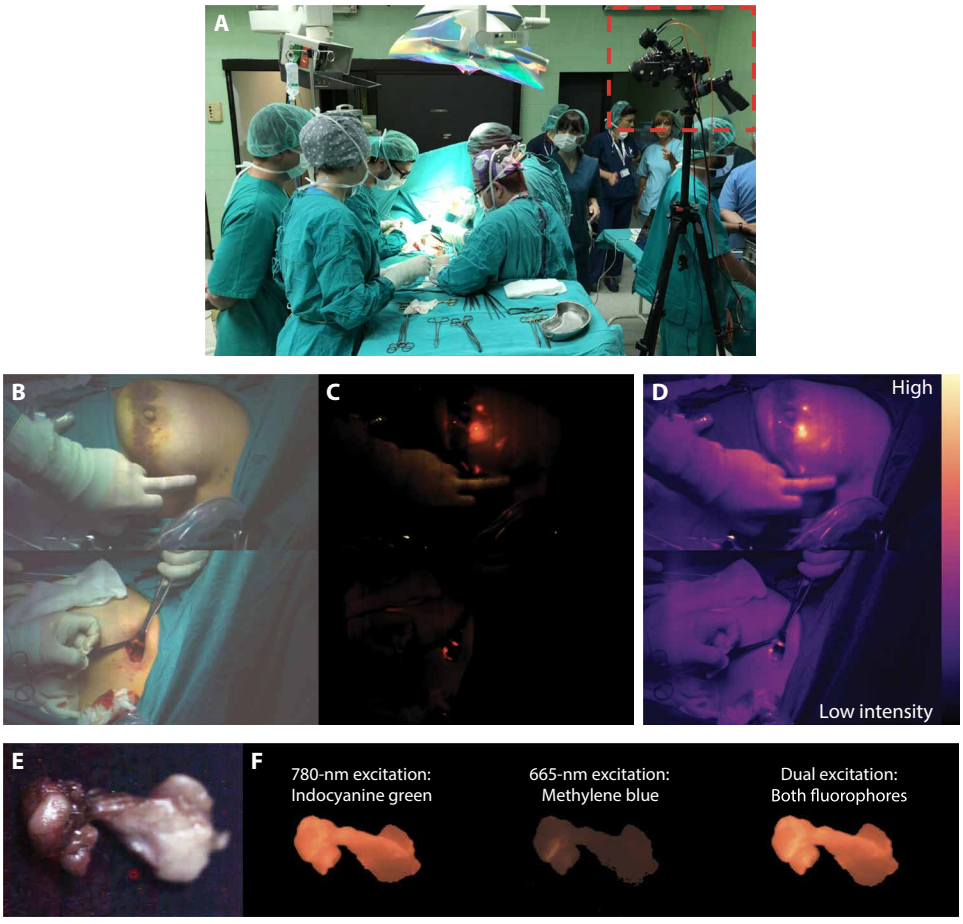

Fig. 5. Clinical feasibility study using the bioinspired imaging sensor to map sentinel lymph nodes. (**A**) Color photograph of the imaging system (red box, top right) integrated into the operating room. (**B** to **D**) In vivo images before and after the surgical incision to remove lymph nodes from a patient with breast cancer; the fluorophores indocyanine green (ICG) and methylene blue (MB) were administered by injection at the surgical site (see movie S2). (B and C) Color photograph (B) and near-infrared image in trichromatic format (i.e., with spectral discrimination) (C) of the surgical site; the trichromatic formatting presents the individual responses from the three near-infrared channels like a color image, preserving the spectral information. Dye injection points and sentinel lymph nodes exhibit high signal-to-background ratio with no false positives due to specular reflections. (D) Near-infrared image in monochromatic format (i.e., without spectral discrimination) of the surgical site; the monochromatic formatting presents the aggregate response across the three near-infrared channels like an intensity image, eliminating the spectral information. Surgical instruments appear as false positives due to the strong signal from specular reflection. (**E** and **F**) Ex vivo resected lymph node presented as a color photograph (E) and as near-infrared images (F) representing ICG alone (left), MB alone (middle), and both dyes together (right). The two dyes accumulate differently in different tissue sites. In vivo images are representative of 7 patients; ex vivo images are representative of 49 resected lymph nodes collected from 11 patients.

DISCUSSION

When successfully translated to the medical field, new sensing technologies can decrease patients' medical expenses and increase their quality of life. In most hospitals, the primary sensing modalities during surgical procedures are the surgeon's eyesight and touch, leading to subjective discrimination between cancerous and healthy tissues. As a result, there is continued interest in the development of imaging systems that can eliminate the positive tumor margins associated with tumor regrowth and the overly negative tumor margins associated with iatrogenic effects. Unfortunately, the adoption of imaging technologies into the operating room has faced little success. The imaging architectures that have come to dominate within the past 50 years of semiconductor and optical research have produced biomedical imaging systems that are incompatible with the clinical environment and thus lack diagnostic performance under operative conditions (*8*–*10*).

Here, we have presented a bioinspired image sensor with hexachromatic vision for image-guided surgical applications. The sensor, which is constructed from arrays of vertically stacked photodetectors and pixelated spectral filters, enables the differentiation of multiple fluorophores across a surgical site without slowing down or otherwise impeding a surgeon's workflow. Near-infrared images are inherently co-registered with visible images in time and space because of this architecture, eliminating the ambiguity between anatomical features and fluorescently labeled structures. Tumor detection in a preclinical mouse model of human prostate cancer indicated that this technology could exploit tumor-targeted markers to enhance resection of multifocal, multicentric, and infiltrative cancers. Sentinel lymph node detection for the clinical management of breast cancer in the operating room demonstrated that this technology could detect such markers against a complex background and elucidate their heterogeneous response. With its compact footprint and low weight, which permit seamless integration into the operating room, our bioinspired imager offers opportunities for quality-based health care as contrast agents continue to evolve.

Recent progress in scientific CMOS image sensors has enhanced optoelectronic performance, with some sensors offering sub-electron read noise. Continuous refinement to the CMOS fabrication and post-CMOS integration of these image sensors and their color filter arrays has also facilitated pixels approaching submicrometer pitches. A previously underexplored technology, stacked photodiode CMOS image sensors have not seen the full benefit of the scientific CMOS image sensor's improvements. Nevertheless, circuit-, system-, and process-level similarities between the two sensors indicate that the largest hurdle to equalizing performance is economic, not scientific (*29*). Comparing a conventional spectrometer to our imager, there is additional concern that the similarities in the quantum efficiencies for the three near-infrared channels as well as the limited magnitudes of those quantum efficiencies at longer wavelengths may negatively affect sensitivity to and discrimination between near-infrared fluorophores. These characteristics have not inhibited our ability to discriminate between common fluorophores, but additional work will be required to identify our sensor's spectral limits as new fluorophores emerge. In its current state, our stacked

Table 1. Clinical feasibility study with the bioinspired imaging sensor to map sentinel lymph nodes. Receiver operating characteristic analysis for sentinel lymph node mapping using indocyanine green in 11 patients with breast cancer undergoing surgical resection ($n_{lymph} = 49$, $n_{non\text{-}lymphatic} = 6$). The optimum true-positive rate and the optimum false-positive rate were evaluated at the threshold with maximal Youden's index.

Estimate	Mean	95% confidence interval
Area under the curve	88%	77.9–96.6%
Optimum true-positive rate	84%	73.5–93.9%
Optimum false-positive rate	0%	0–0%

photodiode imaging system poses solutions to important clinical problems, and with additional improvements, the ability to detect fluorophores at lower concentrations, distinguish fluorophores with closer emission spectra, and capture information in two stacked photodiode pixels that would normally require six conventional pixels should advance patient outcomes. Throughout this transition, our imaging system should further enable lines of inquiry that have previously faced technical obstacles.

One such area of exploration is in multifluorophore detection of sentinel lymph nodes, which was investigated as a part of our clinical study. Early instances of sentinel lymph node mapping used either a blue dye or a radiotracer, whereas modern guidance suggests that both agents should be used to improve identification rates and reduce false-negative rates (*30*, *31*). Likewise, early studies into sentinel lymph node staging used a single targeted agent to highlight metastatic lymph nodes, but recent research indicates that paired agents should be used to improve sensitivity and specificity (*32*–*34*). However, there have been no clinical studies exploring the complementary use of multiple fluorophores for either sentinel lymph node mapping or sentinel lymph node staging. For example, ICG and MB migrate to lymph nodes via the same mechanisms, namely, drift and diffusion from the injection site through the lymphatic capillaries. However, ICG and MB exhibit notable physiochemical differences, with ICG (775 Da) and HSA (66.5 kDa) forming large complexes and MB (320 Da) experiencing no such interaction with serum proteins. Although the literature largely treats the two fluorophores as equivalent for sentinel lymph node mapping, these similarities and differences cause them to accumulate in a correlated, but not identical, manner in lymph nodes—a distinction that may carry subtle but meaningful diagnostic information. If fluorescence image-guided sentinel lymph node biopsy is to enter practice, clinicians must understand whether such complementary use can offer sustained improvements and how it can be properly translated, using both nonspecific and tumor-targeted probes. Our study did not fully explore these possibilities as it only looked at those nonspecific probes available in the clinic as they are used in the standard of care since tumor-targeted probes have not yet received regulatory approval. Nevertheless, imaging systems like ours that are equipped for multifluorophore detection can enable both the fundamental studies into probe pharmacokinetics and the practical studies into patient outcomes needed to understand and evaluate these techniques as the field advances.

Another area of exploration is in three-dimensional reconstruction of surgical sites, which could not be investigated as a part of our clinical study. In remote surgeries or minimally invasive surgeries where the physician cannot directly view the surgical site, simultaneous three-dimensional profilometry and fluorescence imaging obviates the need for the physician to mentally map the surgical volume from multiple video streams on a flat-screen display, whereas in ordinary open surgeries, co-registration of the tissue's profile with its fluorescence frees the surgical staff from the need to constantly turn from the patient to a display. It is unclear how markedly three-dimensional imaging and fluorescence imaging, when combined in this way, would affect surgical outcomes. Surgeons may experience reduced learning curves for some procedures, observe improved standardization in other procedures, and receive new views of surgical sites that enable previously unidentified treatment approaches, but relevant technologies have been rare and underutilized and relevant studies have faced limitations and yielded inconsistent results (*35*). Our study did not examine whether surgical performance differed based on the presence or absence of a three-dimensional profile, but imaging systems like ours can facilitate this line of inquiry. In open surgeries, our imaging system can be integrated with a near-infrared projector in the surgical lighting system to enable three-dimensional reconstruction of the full surgical field, whereas in minimally invasive surgeries, our imaging system can be integrated with a near-infrared light channel and a microelectromechanically actuated grating in an endoscopic lighting system to enable similar reconstruction of the surgical cavity.

MATERIALS AND METHODS

Study design

The goal of this study was to develop a camera based on the compound eye of the mantis shrimp and to apply this camera for multifunctional imaging during cancer surgery. The camera's development was verified by optoelectronic characterization, whereas its application involved two series of experiments. The first series of applied experiments established that the camera could record multiple fluorophores and extract the complementary information encoded in their combined fluorescence. This included benchtop experiments that evaluated whether the emission spectra of various fluorophores could be distinguished and animal experiments that tested whether tumor detection with two tumor-targeted fluorescent probes was superior to that with only one tumor-targeted fluorescent probe. The second series of applied experiments established that the camera could function in the operating room, providing features that were conducive to clinical translation and performance that was equivalent to the current standard of care. This included a benchtop experiment that evaluated whether the excitation spectrum and emission spectrum of a fluorophore could be distinguished and a human study that tested whether sentinel lymph node mapping with near-infrared fluorescent dyes was non-inferior to that with two dark colored dyes and a radiotracer. Additional experiments also explored three-dimensional profilometry with structured illumination and intraoperative imaging during surgical workflows.

Surgeons were blinded to our technology during resection. Analysts were not blinded to the tissue's histopathological status during data processing; instead, statistical methods like cross-validation were used to mitigate overfitting and related effects. Randomization was not necessary given that all animals and patients underwent the same procedures.

All animal experiments were performed under protocols approved by the University of Illinois Institutional Animal Care and Use Committee. The experiments complied with all relevant ethical regulations. All human studies were performed under protocols approved by the Institutional Review Board at the University of Illinois at Urbana-Champaign and the Agency for Drugs and Medical Instruments in Skopje, Republic of North Macedonia; the clinical studies were registered on clinicaltrials.gov (trial ID no. NCT03619967). The studies complied with all relevant ethical regulations and adhered to approved guidelines. All patients gave informed consent before joining this Health Insurance Portability and Accountability Act-compliant study. Inclusion criteria included the following: early or progressive stage of breast cancer and ability to understand and willingness to sign written informed consent documents. Exclusion criteria included the following: presence of inflammatory cancerous tissue, history of allergic reactions to iodide or seafood, failure to detect sentinel lymph nodes with radiocolloid and static gamma camera, history of breast surgery, pregnancy, and unwillingness to enter study.

Animal experiments

Male nude athymic J:NU mice (2 to 3.5 months old, >30 g each; The Jackson Laboratory) were used for in vivo tumor imaging and ex vivo ROC analysis. PC3 and LNCaP cells were incubated, grown to 90% confluence, detached, suspended in Matrigel (Corning), and delivered via subcutaneous injection. The suspension consisted of 2×10^7 cells per 100 μl of 10% Matrigel, and the injection was composed of 50 μl of cell-Matrigel solution. For some mice, two subcutaneous injections of LNCaP cells on the left flank and two subcutaneous injections of PC3 cells on the right flank were delivered. For the remaining mice, two subcutaneous injections of PC3 cells, one on each flank, were delivered. The mice were monitored daily for tumors and were imaged when tumors grew to ~1 cm diameter.

Twenty-four hours before imaging, the animals were anesthetized with 1 to 2% isoflurane, and their skin was prepared using an alcoholic iodine solution and opened during a jugular vein cut-down procedure. For each mouse, two fluorophores were injected in sequence: 200 μl of IRDye 800CW 2-DG (0.1 nmol/1 μl) (labeled with 2-deoxy-D-glucose) followed by 100 μl of IRDye 680RD EGF (2 nmol/100 μl) (labeled with human recombinant epidermal growth factor). Using a surgical microscope for direct visualization, each fluorophore was administered using a 30-gauge insulin syringe needle inserted into the jugular vein. After injection, gentle pressure was applied to the injection site with a cotton-tip swab for about 30 s before the skin was closed with a sterile 6-0 Prolene suture. All procedures were done under aseptic conditions.

At imaging time, the mice were anesthetized under 1 to 2% isoflurane on a heated bed; in vivo images were captured; the surgeon euthanized the mice and removed tissue samples, marking each as either cancer-positive tumor or cancer-negative muscle; and ex vivo images were captured. To mimic the case where IRDye 800CW 2-DG alone was administered, ~20 mW/cm^2 intensity of 780-nm excitation was provided; to mimic the case where IRDye 680RD EGF alone was administered, ~20 mW/cm^2 intensity of 665-nm excitation was provided; and to observe both IRDye 800CW 2-DG and IRDye 680RD EGF, both excitations were provided. The imaging system and excitation sources were set up at a ~0.5-m working distance. The image sensor was equipped with a Canon EF 50mm f/1.2 lens that was focused on the sample and adjusted to an aperture between ~f/2.0 and ~f/4.0. The imaging system was configured to provide a ~200- to ~400-ms exposure for the near-infrared pixels to ensure high signal-to-noise ratio in the fluorescence signal. A total of seven mice were involved, and a total of 48 tissue samples were collected; these tissue samples included 24 tumor tissues (14 PC3 and 10 LNCaP) and 24 healthy tissues.

A multistep procedure was required to locate the tissue sample, extract the near-infrared features, and distinguish the tumor tissues from healthy tissues. Raw images were demosaiced and temporally averaged, and regions of interest corresponding to the tissue samples were selected by hand; these regions were spatially averaged. Near-infrared channels were then mapped from RGB to HSV representations; ultimately, the value (intensity information) was dropped during the classification procedure because the hue and saturation (spectral information) provided sufficient information about the tissue samples. Generation and analysis of ROC curves then followed the procedures described in the "Statistical analysis" section.

Human study

Women with breast cancer undergoing concurrent curative surgery and sentinel lymph node dissection were recruited for in vivo imaging and ex vivo imaging. Before the surgical procedure, ^{99m}Tc-HSA colloid (via Senti-Scint; 834 μCi), ICG (2 ml at 0.5 mg of ICG per milliliter of saline), and MB (1 ml at 10 mg of MB per milliliter of water) were injected into the patient's tumor area, followed by 5 min of site massage; at 10 to 15 min after injection, the surgeon proceeded with the surgery per standard of care. When suspected sentinel lymph nodes were identified using the radioactivity measured with a gamma probe (Europrobe, EuroMedical Instruments) and the visible contrast provided by MB and ICG, the tissues were removed. All resected samples were analyzed using histopathology to confirm or disaffirm sentinel lymph node status.

For one set of patients (seven patients; mean ± SD age: 58 ± 12 years), images of tissues before and during resection were captured. Under operating conditions, bright light from broadband surgical lamps, ~10 mW/cm^2 from a 780-nm laser, and ~10 mW/cm^2 from a 665-nm laser were provided. The image sensor was configured to provide a 25-ms exposure for color pixels and a ~100- to ~200-ms exposure for near-infrared pixels and was equipped with a Canon EF 50mm f/1.2 lens adjusted to an aperture of ~f/2.2. The imaging system and excitation sources were set up at a ~2-m working distance. These in vivo samples were not incorporated into the ROC analysis. For the remaining patients (11 patients; mean ± SD age: 61 ± 15 years), images of tissues after resection were captured. To mimic the case where ICG alone was administered, ~5 mW/cm^2 intensity of 780-nm excitation was provided; to mimic the case where MB alone was administered, ~5 mW/cm^2 intensity of 665-nm excitation was provided; and to observe both the ICG and MB, both excitations were provided. The image sensor was configured to provide a ~200-ms exposure for near-infrared pixels and was equipped with a Rokinon 50mm f/1.4 lens adjusted to an aperture of ~f/2.0. The imaging system and excitation sources were set up at a ~0.5-m working distance. These ex vivo samples were incorporated into the

ROC analysis: 55 tissue samples were collected, of which 49 were lymph nodes and 6 were nonlymphatic structures.

A multistep procedure was required to locate the tissue sample, extract the near-infrared features, and distinguish the sentinel lymph nodes from nonlymphatic structures. Raw images were demosaiced and temporally averaged, and regions of interests corresponding to the tissue samples were selected by isolating a rectangular window at the image's center and extracting the largest contiguous region with average near-infrared response in the 95th percentile and above; these regions were spatially averaged. Near-infrared channels were then mapped from RGB to HSV representations. Generation and analysis of ROC curves then followed the procedures described in the next section.

Statistical analysis

For generation of 95% tolerance ellipses during the fluorescence sensitivity studies, data points were defined as tuples of hues and saturations that laid in a polar coordinate system (i.e., where the hue was the angular coordinate and the saturation was the radial coordinate); however, data points were confined to a sufficiently small region such that the tuples of hues and saturations could be taken to lie in a rectangular coordinate system (i.e., where the saturation was the x coordinate and the hue was the y coordinate). All data points were assumed drawn from a binormal distribution. A 95% tolerance ellipse was taken as an ellipse generated by a method that had an about 95% probability of covering at least 95% of the population when the empirical mean and covariance were taken as sample estimators of the population statistics. As a result, the 95% tolerance ellipse could be computed using equation 5.9 reported in (*36*).

Generation of ROC curves in both the animal and human studies followed similar procedures. To map the near-infrared signal in the hue-saturation–like/HSV-like color space to a classification score appropriate for an ROC analysis without making assumptions on class covariance, quadratic discriminant analysis was used to model probabilities of class membership; to mitigate the risk of overfitting, stratified cross-validation was used in which the dataset was broken into folds with equal class distributions and in which the discriminator was trained on out-of-fold samples and tested on in-fold samples. Conventional algorithms for ROC analysis could then be applied to the cross-validated probabilities to evaluate the AUC for the scorer and to determine the optimal cut point for a classifier.

Statistical analysis of ROC curves was facilitated using a resampling scheme based on the bootstrap method. A family of ROC curves was produced by generating stratified bootstrap samples of the tissue samples and generating ROC curves for each bootstrap sample. Confidence intervals for the AUCs, the true-positive rates, and the false-positive rates were computed using the bias-corrected and accelerated bootstrap interval: A bias-correction parameter related to statistical bias and an acceleration parameter related to statistical skewness were estimated from the dataset and used to correct confidence intervals computed from bootstrapped samples. Confidence intervals were generated at 95% confidence.

Comparison of AUCs was facilitated using a bootstrap-based paired difference test. For each scenario of dye administration, stratified bootstrap samples were generated with the same tissue samples, and ROC curves and AUCs were computed for each bootstrap sample. To compare any two dye administration scenarios, the difference between the AUCs observed over all tissue samples was computed, and the probability under the null hypothesis of the observed difference or a more extreme difference was found by finding the corresponding percentile in the distribution of differences between the paired AUCs observed for the bootstrap samples. These tests were run as one-tailed tests of superiority where, for example, the two-dye administration scenario could be presumed better than the one-dye administration scenario. All tests were run at a significance level of $\alpha = 0.05$.

SUPPLEMENTARY MATERIALS

stm.sciencemag.org/cgi/content/full/13/592/eaaw7067/DC1

Materials and Methods

Fig. S1. Demonstration of the bioinspired imaging system's color reproduction for natural scenes.

Movie S1. Tumor detection in a small-animal model of human prostate cancer showing overlaid information from color images of the mouse, near-infrared images of fluorescently labeled tumors, and three-dimensional shape of mouse and tumors.

Movie S2. Sentinel lymph node mapping in a patient with breast cancer using near-infrared fluorescence from ICG.

Table S1. Optical performance of state-of-the-art near-infrared fluorescence (NIRF) imaging systems compared with our bioinspired NIRF imager.

Table S2. Optical performance of pixelated near-infrared fluorescence (NIRF) imaging systems compared with our bioinspired NIRF imager.

Data file S1. Classification scores from the ROC analysis of tumor detection in a small-animal model of human prostate cancer.

Data file S2. Classification scores from the ROC analysis of sentinel lymph node detection in patients with breast cancer.

References (*37*–*41*)

View/request a protocol for this paper from *Bio-protocol*.

REFERENCES AND NOTES

1. L. V. Wang, J. Yao, A practical guide to photoacoustic tomography in the life sciences. *Nat. Methods* **13**, 627–638 (2016).
2. H. Tu, Y. Liu, D. Turchinovich, M. Marjanovic, J. K. Lyngsø, J. Lægsgaard, E. J. Chaney, Y. Zhao, S. You, W. L. Wilson, B. Xu, M. Dantus, S. A. Boppart, Stain-free histopathology by programmable supercontinuum pulses. *Nat. Photonics* **10**, 534–540 (2016).
3. A. L. Vahrmeijer, M. Hutteman, J. R. van der Vorst, C. J. H. van de Velde, J. V. Frangioni, Image-guided cancer surgery using near-infrared fluorescence. *Nat. Rev. Clin. Oncol.* **10**, 507–518 (2013).
4. S. H. Yun, S. J. J. Kwok, Light in diagnosis, therapy and surgery. *Nat. Biomed. Eng.* **1**, 0008 (2017).
5. R. Daw, J. Finkelstein, Lab on a chip. *Nature* **442**, 367 (2006).
6. G. Hong, A. L. Antaris, H. Dai, Near-infrared fluorophores for biomedical imaging. *Nat. Biomed. Eng.* **1**, 0010 (2017).
7. G. M. van Dam, G. Themelis, L. M. A. Crane, N. J. Harlaar, R. G. Pleijhuis, W. Kelder, A. Sarantopoulos, J. S. de Jong, H. J. G. Arts, A. G. J. van der Zee, J. Bart, P. S. Low, V. Ntziachristos, Intraoperative tumor-specific fluorescence imaging in ovarian cancer by folate receptor-α targeting: First in-human results. *Nat. Med.* **17**, 1315–1319 (2011).
8. A. V. DSouza, H. Lin, E. R. Henderson, K. S. Samkoe, B. W. Pogue, Review of fluorescence guided surgery systems: Identification of key performance capabilities beyond indocyanine green imaging. *J. Biomed. Opt.* **21**, 080901 (2016).
9. R. R. Zhang, A. B. Schroeder, J. J. Grudzinski, E. L. Rosenthal, J. M. Warram, A. N. Pinchuk, K. W. Eliceiri, J. S. Kuo, J. P. Weichert, Beyond the margins: Real-time detection of cancer using targeted fluorophores. *Nat. Rev. Clin. Oncol.* **14**, 347–364 (2017).
10. M. Garcia, C. Edmiston, T. York, R. Marinov, S. Mondal, N. Zhu, G. P. Sudlow, W. J. Akers, J. Margenthaler, S. Achilefu, R. Liang, M. A. Zayed, M. Y. Pepino, V. Gruev, Bio-inspired imager improves sensitivity in near-infrared fluorescence image-guided surgery. *Optica* **5**, 413–422 (2018).
11. G. E. Moore, W. T. Peyton, L. A. French, W. W. Walker, The clinical use of fluorescein in neurosurgery. *J. Neurosurg.* **5**, 392–398 (1948).
12. M. Koller, S.-Q. Qiu, M. D. Linssen, L. Jansen, W. Kelder, J. de Vries, I. Kruithof, G.-J. Zhang, D. J. Robinson, W. B. Nagengast, A. Jorritsma-Smit, B. van der Vegt, G. M. van Dam, Implementation and benchmarking of a novel analytical framework to clinically evaluate tumor-specific fluorescent tracers. *Nat. Commun.* **9**, 3739 (2018).
13. P. S. Low, S. Singhal, M. Srinivasarao, Fluorescence-guided surgery of cancer: Applications, tools and perspectives. *Curr. Opin. Chem. Biol.* **45**, 64–72 (2018).
14. R. L. Siegel, K. D. Miller, A. Jemal, Cancer statistics, 2017. *CA Cancer J. Clin.* **67**, 7–30 (2017).
15. E. R. Fossum, CMOS image sensors: Electronic camera-on-a-chip. *IEEE Trans. Electron Dev.* **44**, 1689–1698 (1997).

16. C. Darwin, *On the Origin of Species by Means of Natural Selection, or, the Preservation of Favoured Races in the Struggle for Life* (John Murray, 1859).
17. Y. M. Song, Y. Xie, V. Malyarchuk, J. Xiao, I. Jung, K. J. Choi, Z. Liu, H. Park, C. Lu, R. H. Kim, R. Li, K. B. Crozier, Y. Huang, J. A. Rogers, Digital cameras with designs inspired by the arthropod eye. *Nature* **497**, 95–99 (2013).
18. H. H. Thoen, M. J. How, T.-H. Chiou, J. Marshall, A different form of color vision in mantis shrimp. *Science* **343**, 411–413 (2014).
19. T. W. Cronin, S. Johnsen, N. J. Marshall, E. J. Warrant, *Visual Ecology* (Princeton Univ. Press, 2014).
20. J. A. Lenero-Bardallo, D. H. Bryn, P. Hafliger, Bio-inspired asynchronous pixel event tricolor vision sensor. *IEEE Ttans. Biomed. Circ. Syst.* **8**, 345–357 (2014).
21. T. York, S. Achilefu, S. P. Lake, B. Raman, V. Gruev, S. B. Powell, S. Gao, L. Kahan, T. Charanya, D. Saha, N. W. Roberts, T. W. Cronin, J. Marshall, Bioinspired polarization imaging sensors: From circuits and optics to signal processing algorithms and biomedical applications. *Proc. IEEE* **102**, 1450–1469 (2014).
22. N. Niikura, J. Liu, N. Hayashi, E. A. Mittendorf, Y. Gong, S. L. Palla, Y. Tokuda, A. M. Gonzalez-Angulo, G. N. Hortobagyi, N. T. Ueno, Loss of human epidermal growth factor receptor 2 (HER2) expression in metastatic sites of HER2-overexpressing primary breast tumors. *J. Clin. Oncol.* **30**, 593–599 (2012).
23. N. J. Marshall, M. F. Land, C. A. King, T. W. Cronin, The compound eyes of mantis shrimps (Crustacea, Hoplocarida, Stomatopoda). I. Compound eye structure: The detection of polarized light. *Philos. Trans. R. Soc. B* **334**, 33–56 (1991).
24. Teledyne QImaging, "MicroPublisher 6™ CCD Camera Datasheet" (2019).
25. H. E. Rhodes, H. Nozaki, S. Manabe, *US2009/0200580A1—Image Sensor and Pixel Including a Deep Photodetector* (Omnivision Technologies Inc., 2009).
26. T. Dai, H.-C. Tai, S. Manabe, H. Nozaki, H. E. Rhodes, *US8228411B2—Circuit and Photo Sensor Overlap for Backside Illumination Image Sensor* (Omnivision Technologies Inc., 2012).
27. International Electrotechnical Commission, Medical electrical equipment—Part 2—41: Particular requirements for the safety of surgical luminaires and luminaires for diagnosis (IEC 60601-2-41:2000) (2000).
28. International Electrotechnical Commission, Safety of laser products—Part 1: Equipment classification, requirements and user's guide (IEC 60825-1:1993+AMD1:1997+AMD2:2001 CSV) (2001).
29. R. M. Turner, R. J. Guttosch, *ICIS '06, International Congress of Imaging Science* (Society for Imaging Science and Technology, 2006), pp. 175–181.
30. G. H. Lyman, A. E. Giuliano, M. R. Somerfield, A. B. Benson III, D. C. Bodurka, H. J. Burstein, A. J. Cochran, H. S. Cody III, S. B. Edge, S. Galper, J. A. Hayman, T. Y. Kim, C. L. Perkins, D. A. Podoloff, V. H. Sivasubramaniam, R. R. Turner, R. Wahl, D. L. Weaver, A. C. Wolff, E. P. Winer; American Society of Clinical Oncology, American society of clinical oncology guideline recommendations for sentinel lymph node biopsy in early-stage breast cancer. *J. Clin. Oncol.* **23**, 7703–7720 (2005).
31. H. S. Cody III, J. Fey, T. Akhurst, M. Fazzari, M. Mazumdar, H. Yeung, S. D. Yeh, P. I. Borgen, Complementarity of blue dye and isotope in sentinel node localization for breast cancer: Univariate and multivariate analysis of 966 procedures. *Ann. Surg. Oncol.* **8**, 13–19 (2001).
32. J. Baeten, J. Haller, H. Shih, V. Ntziachristos, In vivo investigation of breast cancer progression by use of an internal control. *Neoplasia* **11**, 220–227 (2009).
33. E. N. Savariar, C. N. Felsen, N. Nashi, T. Jiang, L. G. Ellies, P. Steinbach, R. Y. Tsien, Q. T. Nguyen, Real-time In vivo molecular detection of primary tumors and metastases with ratiometric activatable cell-penetrating peptides. *Cancer Res.* **73**, 855–864 (2013).
34. K. M. Tichauer, K. S. Samkoe, J. R. Gunn, S. C. Kanick, P. J. Hoopes, R. J. Barth, P. A. Kaufman, T. Hasan, B. W. Pogue, Microscopic lymph node tumor burden quantified by macroscopic dual-tracer molecular imaging. *Nat. Med.* **20**, 1348–1353 (2014).
35. A. Arezzo, N. Vettoretto, N. K. Francis, M. A. Bonino, N. J. Curtis, D. Amparore, S. Arolfo, M. Barberio, L. Boni, R. Brodie, N. Bouvy, E. Cassinotti, T. Carus, E. Checcucci, P. Custers, M. Diana, M. Jansen, J. Jaspers, G. Marom, K. Momose, B. P. Müller-Stich, K. Nakajima, F. Nickel, S. Perretta, F. Porpiglia, F. Sánchez-Margallo, J. A. Sánchez-Margallo, M. Schijven, G. Silecchia, R. Passera, Y. Mintz, The use of 3D laparoscopic imaging systems in surgery: EAES consensus development conference 2018. *Surg. Endosc.* **33**, 3251–3274 (2019).
36. V. Chew, Confidence, prediction, and tolerance regions for the multivariate normal distribution. *J. Am. Stat. Assoc.* **61**, 605–617 (1966).
37. S. Zhang, S.-T. Yau, Generic nonsinusoidal phase error correction for three-dimensional shape measurement using a digital video projector. *Appl. Opt.* **46**, 36–43 (2007).
38. R. M. Goldstein, H. A. Zebker, C. L. Werner, Satellite radar interferometry: Two-dimensional phase unwrapping. *Radio Sci.* **23**, 713–720 (1988).
39. H. Du, Z. Wang, Three-dimensional shape measurement with an arbitrarily arranged fringe projection profilometry system. *Opt. Lett.* **32**, 2438–2440 (2007).
40. Z. Chen, X. Wang, R. Liang, RGB-NIR multispectral camera. *Opt. Express* **22**, 4985–4994 (2014).
41. Z. Chen, N. Zhu, S. Pacheco, X. Wang, R. Liang, Single camera imaging system for color and near-infrared fluorescence image guided surgery. *Biomed. Opt. Express* **5**, 2791–2797 (2014).

Acknowledgments: We thank J. Hutchinson and P. J. Watson for manuscript editing.
Funding: This work was funded by grants from the U.S. Air Force Office of Scientific Research (FA9550-18-1-0278), Congressionally Directed Medical Research Programs (W81XWH-19-1-0299), National Science Foundation (2030421), and Office of Naval Research (N00014-19-1-2400). **Author contributions:** V.G. conceived the idea behind the image sensor and oversaw the entire project. M.G. and V.G. designed the image sensor. Optical evaluation of the image sensor, including optoelectronic characterization and fluorescence sensitivity, was performed by S.B., M.G., T.D., Z.Z., Z.L., and V.G. Cell cultures were maintained by C.K. and W.L.D. Animal studies were designed, performed, and evaluated by S.B., M.G., T.D., C.K., K.K., W.L.D., S.N., and V.G. The three-dimensional reconstruction algorithm was developed and evaluated by S.B., M.G., and T.D. Human studies were designed, performed, and evaluated by S.B., M.G., T.D., R.C., I.F., B.K., S.S., M.B.T., N.T.D., N.J., D.M., G.P., G.K., and V.G. Statistical analysis was provided by S.B. and T.D. The manuscript was written by S.B., M.G., and V.G. All authors proofread the manuscript. **Competing interests:** M.G. and V.G. are listed as coinventors on patent no. US20200120293A1, "Multispectral imaging sensors and systems." The authors declare no other competing interests. **Data and materials availability:** All data associated with this study are present in the paper or the Supplementary Materials.

Submitted 17 January 2019
Resubmitted 22 December 2020
Accepted 14 April 2021
Published 5 May 2021
10.1126/scitranslmed.aaw7067

Citation: S. Blair, M. Garcia, T. Davis, Z. Zhu, Z. Liang, C. Konopka, K. Kauffman, R. Colanceski, I. Ferati, B. Kondov, S. Stojanoski, M. B. Todorovska, N. T. Dimitrovska, N. Jakupi, D. Miladinova, G. Petrusevska, G. Kondov, W. L. Dobrucki, S. Nie, V. Gruev, Hexachromatic bioinspired camera for image-guided cancer surgery. *Sci. Transl. Med.* **13**, eaaw7067 (2021).

Abstract

One-sentence summary: A color/near-infrared camera inspired by the mantis shrimp visual system enables tumor detection and lymph node mapping during cancer surgery.

Editor's Summary:
Through a shrimp eye brightly

A camera for intraoperative imaging of tumors could improve surgical outcomes, but some imaging technologies have been difficult to translate to clinical practice. Blair *et al.* designed an imaging system based on the eye of the mantis shrimp. This system detected multiple near-infrared fluorescent signals simultaneously and was tested in a mouse model of human prostate cancer. In support of clinical feasibility, the authors showed that fluorescently labeled sentinel lymph nodes could be detected by the sensor in patients with breast cancer undergoing surgical resection. This bioinspired imaging sensor could offer a flexible tool for image-guided surgical removal of tumors.